Monthly Notices of the ROYAL ASTRONOMICAL SOCIETY

MNRAS **539,** 1692–1705 (2025) https://doi.org/10.1093/mnras/staf611
Advance Access publication 2025 April 11

Galaxy and halo properties around cosmic filaments from Sloan Digital Sky Survey Data Release 7 and the ELUCID simulation

Youcai Zhang [1]★ Xiaohu Yang,[2,3] Hong Guo,[1] Peng Wang[1] and Feng Shi[4]

[1]*Shanghai Astronomical Observatory, Nandan Road 80, Xuhui District, Shanghai 200030, China*
[2]*State Key Laboratory of Dark Matter Physics, Tsung-Dao Lee Institute, Lisuo Road 1, Pudong New Area, Shanghai 201210, China*
[3]*Shanghai Key Laboratory for Particle Physics and Cosmology, School of Physics and Astronomy, Shanghai Jiao Tong University, Dongchuan Road 800, Minhang District, Shanghai 200240, China*
[4]*School of Aerospace Science and Technology, Xidian University, Xinglong Section of Xifeng Road 266, Chang'an District, Xi'an 710126, China*

Accepted 2025 April 9. Received 2025 April 9; in original form 2025 January 15

ABSTRACT

Using galaxies from the Sloan Digital Sky Survey Data Release 7 (SDSS DR7) along with haloes from the dark matter only constrained ELUCID (Exploring the Local Universe with the reConstructed Initial Density field) simulation, we examine the properties of galaxies and haloes with respect to their distance to cosmic filaments, determined by the medial-axis thinning technique of the COsmic Web Skeleton method. Our findings suggest that galaxies or subhaloes grow in mass as they approach these filaments. Galaxies exhibit a redder colour and diminished specific star formation rates as they approach these filaments. Additionally, older subhaloes tend to be more common near the central regions of these filaments. Elliptical galaxies are more frequently found than spiral galaxies in the central regions of the filaments. Lower mass galaxies typically display reduced sizes in proximity to filaments, whereas higher mass galaxies tend to exhibit increased sizes when close to filaments. Moreover, the concentration and spin of the haloes grow as they approach the filaments. These findings support the notion that the large-scale structure of Universe, characterized by cosmic web structures, plays a vital role in shaping galaxy and halo properties.

Key words: methods: statistical – large-scale structure of Universe – cosmology: observations.

1 INTRODUCTION

In the framework of hierarchical structure formation, galaxies are believed to form within dark-matter haloes, which reside in a vast and intricate network known as the cosmic web (Bond, Kofman & Pogosyan 1996; Cautun et al. 2014). According to the distribution of galaxies observed in redshift surveys (DESI Collaboration 2024) and dark matter mapped in cosmological simulations (Pakmor et al. 2023), the cosmic web consists of knots, filaments, sheets, and voids that form due to gravitational instability from primordial density fluctuations (Peebles 1967). Consequently, the properties of galaxies and haloes are anticipated to be influenced by the cosmic web environment. The intricate and fascinating interactions between galaxies, dark-matter haloes, and their surrounding cosmic web present a complex challenge in understanding galaxy formation and evolution (Wechsler & Tinker 2018; Zhang, Yang & Guo 2021a,b; Romeo, Agertz & Renaud 2023; Montero-Dorta & Rodriguez 2024; Wang et al. 2024a,b).

In recent decades, numerous studies have shown that galaxy properties are influenced not only by their immediate halo environments but also by the larger cosmic web. On halo scales, galaxies generally exhibit lower star formation rates (SFRs), redder colours, and more elliptical shapes in dense regions (Woo et al. 2013; Old et al. 2020). However, Taamoli et al. (2024) found that galaxies in dense environments have increased star formation activity at redshifts greater than $z > 2$. On larger scales, galaxies typically experience quenching within cosmic filaments or sheets (Salerno et al. 2020; Pasha et al. 2023), although Hasan et al. (2023) suggested that the specific star formation rate (sSFR) does not depend on the cosmic web environment at $z \geq 2$.

The influence of cosmic web environments on galaxy formation and evolution remains a topic of active discussion (Donnan, Tojeiro & Kraljic 2022; Rosas-Guevara et al. 2022; Domínguez-Gómez et al. 2023). Galaxies are embedded in a complex cosmic web marked by elongated thread-like filaments that extend between massive clusters and enclose mostly vacant regions of space known as voids. Many studies have asserted that galaxies located in voids demonstrate higher SFRs and show bluer colours relative to those in dense environments, with this pattern being especially evident among low-mass galaxies (Hoyle et al. 2005; Hoyle, Vogeley & Pan 2012; Conrado et al. 2024; Curtis, McDonough & Brainerd 2024; Parente et al. 2024). However, various research findings indicate that the void environment does not significantly affect galaxy properties (Kreckel et al. 2015; Wegner et al. 2019). Alpaslan et al. (2015) analysed environmental catalogues from the Galaxy And Mass Assembly (GAMA) survey (Alpaslan et al. 2014) and found that stellar mass, rather than environmental classification, predominantly affects galaxy properties. They found that, when controlling for mass, galaxies display similar properties such as effective radius, morphology, and $u - r$ colour, independent of the large-scale environment. In contrast, this study supports the view that the large-scale environment plays a vital role in shaping galaxy

★ E-mail: yczhang@shao.ac.cn

characteristics by analysing the properties of galaxies near cosmic filaments.

Filaments, as the most prominent visual entities in the cosmic web, can act as channels for matter to flow into clusters (Kleiner et al. 2017; Lu et al. 2024; Rowntree et al. 2024). In recent years, various methodologies have been developed to detect cosmic filaments through geometric or topological analysis of particle distributions, such as DisPerSE (Sousbie 2011; Sousbie, Pichon & Kawahara 2011); by using Hessian matrices of density, tidal or velocity shear tensors, such as the NEXUS algorithm (Cautun, van de Weygaert & Jones 2013); and through machine learning techniques, such as the Subspace-Constrained Mean-Shift algorithm (Carrón Duque et al. 2022). Generally, these filament detection algorithms are created for different study objectives.

Employing filament detection methods, numerous studies have explored cosmic filaments to understand their influence on the formation and evolution of galaxies (Darvish et al. 2014; Sarron et al. 2019; Vulcani et al. 2019; Parente et al. 2024). A key area of interest is how the properties of galaxies vary with respect to their distance to the filament axes. Many studies suggest that galaxies often exhibit an increase in stellar mass as they approach filaments based on both simulations (Bulichi, Davé & Kraljic 2024) and observational data (Chen et al. 2017; Malavasi et al. 2017; Hoosain et al. 2024). In contrast, Kuutma, Tamm & Tempel (2017) found no evidence of an increase in galaxy stellar mass close to filaments, using a filament catalogue generated via the Bisous model point process from Sloan Digital Sky Survey Data Release 10 (SDSS DR10).

Apart from the dependence on stellar mass, galaxies near filaments show redder colours and lower rates of star formation (Tugay & Tarnopolski 2023), which is confirmed by the filament catalogues generated using the DisPerSE algorithm in various surveys, such as the GAMA survey for $0.02 < z < 0.25$ (Kraljic et al. 2018), the Cosmic Evolution Survey (COSMOS) for $0.5 < z < 0.9$ (Laigle et al. 2018), the COSMOS *H I* Large Extragalactic Survey (CHILES) for $0 < z < 0.45$ (Luber et al. 2019), the SDSS for $z \sim 0.1$ (Winkel et al. 2021), and the combined data sets from the Wide-field Infrared Survey Explorer (WISE) and SuperCOSMOS for $0.1 < z < 0.3$ (Bonjean et al. 2020). However, Bulichi et al. (2024) found that the quenching of star formation near filaments vanishes, and instead, there is a rise in SFRs near filaments at $z = 2$ for filament catalogues identified with the DisPerSE algorithm in the SIMBA simulation. Based on the IllustrisTNG simulation, Hasan et al. (2024) asserted that the median sSFR relative to the distance to the filament axes depends on the technique used to generate the density field in the DisPerSE algorithm. According to Hasan et al. (2024), the employment of the Delaunay Tessellation Field Estimator (DTFE) to analyse galaxies reveals a decrease in star formation in galaxies that are proximate to filaments. In contrast, filaments determined by the Monte Carlo Physarum Machine (MCPM) method seem to have little influence on star-forming activities. The observed differences between the DTFE and MCPM methods stem from the way they each identify filamentary structures. The MCPM density field, when used with the DisPerSE method, excels at detecting less prominent filaments that the DTFE density construction method tends to miss.

Galaxy sizes represent a vital observational aspect crucial for enhancing theories on galaxy evolution. Jiang et al. (2019) utilized data from two separate cosmological hydrodynamical simulations, revealing that the size of a galaxy does not depend on the halo spin but inversely correlates with the halo concentration. Considering the substantial influence of cosmic filaments on spin orientation (Zhang et al. 2009, 2013, 2015), it is intriguing to examine how galaxy and halo sizes, in addition to halo spin and concentration, change relative to their distance from the filament.

This study mainly examines how the properties of galaxies and haloes change with respect to their proximity to the filament axes. The galaxy characteristics analysed are stellar mass, ${}^{0.1}g - r$ colour indices, sSFR, and half-light radius R_{50}, along with the ratio of elliptical to spiral galaxies (E/S ratio). For haloes, this research focuses on the subhalo mass, the redshift of the formation of the subhalo, the half-mass radius of the halo $R_{1/2}$, the virial radius of the halo $R_{\rm vir}$, the spin parameter of the halo λ and the concentration of the halo $c_{\rm vir}$.

One approach to grasp the characteristics of galaxies and haloes in relation to filaments is to employ a simulation that is designed based on the real observed density field of galaxy distribution. With the help of the constrained ELUCID simulation, observed galaxies can be efficiently linked to dark matter haloes within the simulation (Yang et al. 2018). The topology and geometry of the cosmic web in simulation are precisely mirrored in comparison to actual observations, as the initial conditions of the ELUCID simulation are constrained by the group mass density field from SDSS DR7 (Yang et al. 2007, 2012; Wang et al. 2012, 2014, 2016, 2018).

The characteristics of filaments are shaped not only by the identification methods used but also by the different tracers, such as dark-matter particles and galaxies (Malavasi et al. 2020; Rost et al. 2020; Zakharova et al. 2023; Zhang et al. 2024). In this study, we employ dark matter particles from the ELUCID simulation to detect cosmic web filaments using the COsmic Web Skeleton (COWS) technique (Pfeifer et al. 2022). Applying a medial axis thinning algorithm (Zhang & Suen 1984; Lee, Kashyap & Chu 1994), cosmic filaments are identified within the cosmic web environment classified by the Hessian matrix of the density field (Zhang et al. 2024). Based on the filament catalogues extracted from the ELUCID simulation, this study investigates the variation in properties of galaxies and haloes relative to their distances to filament axes, using galaxies from SDSS DR7 and haloes in the simulation.

The structure of this paper is organized as follows. Section 2 describes the observational data from SDSS DR7 and the simulation data from the ELUCID simulation. Additionally, we explain the COWS filament finding technique and the approach used to match observed galaxies with haloes in the constrained simulation. Section 3 explores how the properties of galaxies and haloes depend on their distance to filaments. Finally, Section 4 summarizes our findings. In this study, we adopt the cosmological parameters from the ELUCID simulation: $\Omega_m = 0.258$, $\Omega_b = 0.044$, $\Omega_\Lambda = 0.742$, $h = 0.72$, $n_s = 0.963$, and $\sigma_8 = 0.796$.

2 DATA AND METHOD

2.1 Observational data

The galaxy data set used in this research is sourced from the SDSS (York et al. 2000; Abazajian et al. 2009), known as one of the most significant astronomical surveys. Blanton et al. (2005) utilized multiband imaging along with SDSS DR7 spectroscopic data to build the New York University Value-Added Galaxy Catalogue (NYU-VAGC), which features enhancements over the public releases of the SDSS. The NYU-VAGC catalogue is more appropriate for studying large-scale structure statistics because it reduces systematic calibration errors. From the NYU-VAGC, we collected a total of 639 359 galaxies with redshifts in the range $0.01 \leq z \leq 0.2$, redshift completeness $\mathcal{C}_z > 0.7$, and apparent magnitudes brighter than $r \leq 17.72$. The criteria for selecting galaxies ensure both reliable

r-band magnitudes and precise redshift measurements. In addition, the selection criteria ensure that most of the galaxies selected are included in the group catalogue identified via the halo-based group finder from SDSS DR7 (Yang et al. 2007, 2012). This catalogue is fundamental for developing the reconstructed initial conditions for the ELUCID simulation (Wang et al. 2016).

The galaxy stellar mass M_* is derived using the mass-to-light ratio and colour correlation as described by Bell et al. (2003), which is given by the equation

$$\log\left(\frac{M_*}{h^{-2}M_\odot}\right) = -0.306 + 1.097[^{0.0}(g-r)] - 0.1 - 0.4(^{0.0}M_r - 5\log h - 4.64), \quad (1)$$

where $^{0.0}(g-r)$ and $^{0.0}M_r - 5\log h$ represent the $(g-r)$ colour and r-band magnitude corrected for $K+E$ at $z=0.0$, with 4.64 being the r-band magnitude of the Sun in the AB magnitude system, and the -0.10 factor indicating the use of a Kroupa (2001) initial mass function.

The galaxy SFRs are sourced from the public catalogue of Chang et al. (2015), which includes reliable aperture corrections. They combine SDSS and WISE (Wright et al. 2010) photometry for the entire SDSS spectroscopic galaxy sample to construct spectral energy distributions (SEDs). Chang et al. (2015) employ the Multiwavelength Analysis of Galaxy Physical Properties (MAGPHYS;[1] da Cunha, Charlot & Elbaz 2008) technique to coherently and systematically model both the attenuated stellar SED and the dust emission. This approach enables more reliable estimations of galaxy SFRs by considering emissions from polycyclic aromatic hydrocarbons as well as thermal dust radiation. The stellar masses listed in the public catalogue are also used to explore the relationship between the mass of galaxies and their proximity to filament spines. Overall, the principal conclusions remained stable despite the variations in the stellar mass applied.

The morphological classifications of galaxies originate from the Galaxy Zoo 2 catalogue (GZ2;[2] Willett et al. 2013), which uses classifications from volunteer citizen scientists to measure morphologies for galaxies in the SDSS DR7 Legacy Survey with apparent magnitudes $r \leq 17$. A multilevel decision tree was used to classify galaxy morphologies, drawing on inputs from citizen scientist classifiers through an online platform. The comprehensive catalogue includes morphological classifications for 304 122 galaxies, each galaxy being associated with strings identified as $gz2\_class$. Galaxies classified as elliptical and spiral are represented by $gz2\_class$ strings that start with 'E' and 'S', respectively. The data set generated by matching the GZ2 catalogue with the NYU-VAGC catalogue comprises 107 230 elliptical galaxies and 134 024 spiral galaxies.

Galaxy sizes are obtained from the NYU-VAGC catalogue within the table *object_sdss_imaging.fits*, focussing on the r-band radii denoted as R_{50}, which encompass 50 per cent of the Petrosian flux. The Petrosian flux F_P for any band is the flux within a certain number N_P ($N_\mathrm{P}=2.0$ in the SDSS) of the Petrosian radius r_P, and is given by

$$F_\mathrm{P} = \int_0^{N_\mathrm{P} r_\mathrm{P}} 2\pi r I(r)\mathrm{d}r, \quad (2)$$

where $I(r)$ is the average surface brightness in relation to radius, and r_P is the radius at which the Petrosian ratio R_P reaches a specified limit ($R_\mathrm{P}=0.2$ in the SDSS). The ratio R_P is defined as the ratio of the local surface brightness in an annulus to the mean surface brightness within the radius r_P, expressed by (Blanton et al. 2001)

$$R_\mathrm{P} = \frac{\int_{0.8r_\mathrm{P}}^{1.25r_\mathrm{P}} 2\pi r I(r)\mathrm{d}r / \left[\pi\left(1.25^2 - 0.8^2\right) r_\mathrm{P}^2\right]}{\int_0^{r_\mathrm{P}} 2\pi r I(r)\mathrm{d}r / \left(\pi r_\mathrm{P}^2\right)}. \quad (3)$$

In general, the galaxy sizes listed in the NYU-VAGC catalogue agree well with those reported in the public catalogues by Simard et al. (2011) and Meert, Vikram & Bernardi (2015), particularly for galaxies with lower masses (Zhang, Yang & Guo 2022). Unless mentioned otherwise, the galaxy sizes from the NYU-VAGC catalogue are used throughout the paper.

2.2 Simulation data

The ELUCID simulation, which focusses only on dark matter, is a constrained simulation capable of replicating the density field of the nearby Universe (Wang et al. 2012, 2014, 2016). These reconstructions are constrained by the distribution of dark-matter haloes, which are represented by galaxy groups exceeding a mass of $10^{12}\,h^{-1}\mathrm{M}_\odot$, based on data from the SDSS redshift survey (Yang et al. 2007, 2012).

The initial conditions for the density field stem from reconstruction techniques that utilize the halo domain approach and the Monte Carlo Hamiltonian Markov chain method (HMC) (Wang et al. 2012, 2014). In the context of the HMC framework, Fourier modes are specifically created for smaller k values, which correspond to larger scales, with a particular focus when $k \leq \pi/l_g$, where l_g denotes the grid cell size used in the HMC process. Random phases are used to compensate for the absence of higher k modes, which represent smaller scales. Therefore, about 95 per cent of the galaxy groups with masses exceeding $10^{14}\,h^{-1}\mathrm{M}_\odot$ can be accurately aligned with simulated haloes of comparable masses, allowing a distance error of up to $4\,h^{-1}$Mpc (Wang et al. 2016; Chen et al. 2019). Massive structures such as the Coma cluster and the Sloan Great Wall are effectively replicated in this reconstruction (Luo et al. 2024). However, caution must be exercised when employing small-scale structures from the ELUCID simulation to depict observed galaxy distributions (Tweed et al. 2017).

The simulation begins with an initial condition sampled using 3072^3 dark-matter particles at a redshift of $z=100$ within a periodic box measuring $500\,h^{-1}$Mpc per side. The density field subsequently evolved to the current epoch using a memory-efficient version of Gadget-2 (Springel 2005). Throughout the simulation, 100 snapshots are generated, ranging from redshift $z=18.4$ to $z=0$, with the expansion factor distributed in logarithmic intervals. Each dark matter particle has a mass of $3.1\times10^8\,h^{-1}\mathrm{M}_\odot$.

In the simulation, the conventional friends-of-friends (FOF) algorithm (Davis et al. 1985) is applied to the particle data to create FOF haloes with a linking length of $b=0.2$ times the average particle separation. Subsequently, the SUBFIND algorithm (Springel et al. 2001) breaks down a given FOF halo into a collection of separate subhaloes with gravitational bind during the unbinding process, where the gravitational potentials are computed iteratively to eliminate the unbound particles within the host FOF halo. By identifying subhaloes with the SUBFIND algorithm, merger trees are built by connecting a subhalo in one snapshot to its descendant subhalo in the next snapshot. The formation redshift z_f of the subhalo is defined as the redshift when the progenitor of the main branch reached half of its maximum mass M_peak (Zhang, Yang & Guo 2021b).

[1] https://www.iap.fr/magphys/
[2] https://data.galaxyzoo.org/

For each subhalo in the simulation, the dimensionless spin parameter λ is determined using the equation (Peebles 1969)

$$\lambda = \frac{J|E|^{1/2}}{GM_{\rm h}^{5/2}}, \tag{4}$$

where $M_{\rm h}$ refers to the subhalo mass, J signifies the total angular momentum, E indicates the subhalo's total energy, and G is Newton's gravitational constant.

For a halo characterized by a virial radius $R_{\rm vir}$ (Bryan & Norman 1998), the concentration is defined as

$$c_{\rm vir} = \frac{R_{\rm vir}}{r_{\rm s}}, \tag{5}$$

where $r_{\rm s}$ denotes the scale radius in the density profiles, as outlined by the straightforward formula in Navarro, Frenk & White (1997):

$$\frac{\rho(r)}{\rho_{\rm cirt}} = \frac{\delta_{\rm c}}{(r/r_{\rm s})(1+r/r_{\rm s})^2}, \tag{6}$$

where $\rho_{\rm cirt}$ is the critical density of the universe, and $\delta_{\rm c}$ represents a characteristic density contrast (Zhao et al. 2009; Zhang et al. 2022).

2.3 Algorithm for detecting filaments

The spatial environment at any point is classified into knots, filaments, sheets, and voids employing the Hessian matrix of the density field (Zhang et al. 2009). To build the density field, a cloud-in-cell (CIC) interpolation with 1024^3 cells is applied to 3072^3 dark matter particles in the ELUCID simulation. Subsequently, this field is smoothed using a Gaussian kernel with a width of $R_{\rm s}$ to produce the smoothed density $\rho_{\rm s}$. The Hessian matrix of the smoothed density field, normalized negatively,[3] is defined for each cell of the grid as

$$H_{ij} = -\frac{R_{\rm s}^2}{\rho_{\rm mean}}\frac{\partial^2\rho_{\rm s}}{\partial x_i \partial x_j}, \tag{7}$$

where $\rho_{\rm mean}$ is the average density of the universe. In equation (7), the eigenvalues of the Hessian matrix at the location of each cell are represented by λ_1, λ_2, and λ_3 (ordered such that $\lambda_1 > \lambda_2 > \lambda_3$) with corresponding eigenvectors $\hat{\boldsymbol{e}}_1$, $\hat{\boldsymbol{e}}_2$, and $\hat{\boldsymbol{e}}_3$. The classification of the cosmic web type for each cell is determined by counting how many eigenvalues satisfy $\lambda_i > \lambda_{\rm th}$, where i equals 1, 2, or 3. The classification of the environment is specific to each cell, and the grouping of adjacent cells sharing the same cosmic web-type forms the geometric structures known as voids, sheets, filaments, or knots.

Taking into account the spatial arrangement of the filament cells, the filament axes are determined using the medial axis thinning algorithm implemented in the COWS method (Pfeifer et al. 2022). According to cosmic web classifications, the initial data set is converted into a binary format where knot and filament cells are given a value of 1, while sheets and void cells receive a value of 0. Subsequently, the medial axis thinning algorithm (Lee et al. 1994) is applied to condense the extensive binary data into a single-cell skeleton by detecting and removing border cells while maintaining the geometric and topological characteristics of the data set. Finally, individual filaments are identified by removing extraneous contaminants or features, such as junctions, hollow cavities, and knot cells, from the topological skeleton.

[3]The negative sign on the right-hand side of equation (7) is included to guarantee that positive (negative) eigenvalues correspond to collapsing (expanding) matter. This is consistent with the eigenvalue signs of the tidal tensor in the dynamic model (Hahn et al. 2007).

In previous research (Zhang et al. 2024), we explored the statistical characteristics of filaments using different parameters $R_{\rm s}$ and $\lambda_{\rm th}$. According to Zhang et al. (2024), as the smoothing parameter $R_{\rm s}$ increases, the filament lengths tend to be longer. Moreover, our analysis of the density profiles showed that the filaments generally thicken with increasing $R_{\rm s}$.

Fig. 1 illustrates the distribution of dark matter density and filaments in a $10\,h^{-1}$Mpc slice of the ELUCID simulation, where darker regions represent areas of higher density. The filament spine is detected through the COWS technique, which is based on cosmic web classifications that differ in values $R_{\rm s}$ and $\lambda_{\rm th}$. Fig. 1 compares filament axes determined with different parameters: the top panels illustrate these axes using a smoothing length of $R_{\rm s} = 2.1\,h^{-1}$Mpc with thresholds $\lambda_{\rm th} = 0.2$ and 0.8, while the bottom panels present results for $R_{\rm s} = 4.0\,h^{-1}$Mpc. Generally, the filament axes are closely aligned with most of the visible filamentary structures in the darker regions.

To determine the corresponding positions in the ELUCID simulation that align with the observed locations of galaxies, the galaxies' observable coordinates (α, δ, z) are transformed into the simulation's (X, Y, Z) coordinate system using the following equations:

$$\begin{aligned} X &= R(z)\cos\delta\cos\alpha \\ Y &= R(z)\cos\delta\sin\alpha \\ Z &= R(z)\sin\delta, \end{aligned} \tag{8}$$

where α is the right ascension, δ is the declination, and $R(z)$ is the comoving distance corresponding to redshift z. Fig. 2, similar to Fig. 1, shows the COWS filaments overlaid on the galaxy distribution. Here, the observed galaxy positions have been transformed into the coordinate framework of the ELUCID simulation. Typically, the axes of the filaments are nearly parallel to the filamentary structures outlined by the distribution of galaxies.

Consider a defined neighbourhood around a specific cell, such as the 26 neighbourhoods N_{26}, which includes all adjacent cells within a $3 \times 3 \times 3$ cube, covering all direct, diagonal, and corner neighbours. Lee et al. (1994) introduced a technique to identify the cells that make up the skeleton by counting the neighbours that each cell possesses in N_{26}. Cells with 1, 2, 3, and 4 neighbours are classified as end points, regular cells, T junctions, and X junctions, respectively. For the purpose of skeleton classification, each cell is assigned a number corresponding to the count of neighbouring cells in N_{26}. Cells possessing more than two neighbours are removed. Filaments can be detected by recursively connecting cells within N_{26}, beginning from a cell marked as an endpoint and continuing until another endpoint is encountered, which means that no further cells can be linked. Observe that each filament detected by the COWS method has two endpoints linked by a single path with a width of one cell. This configuration allows for the calculation of how galaxy properties vary with the distance perpendicular to the filament axes.

Clearly, the medial axis thinning algorithm used to detect filaments in cosmic web catalogues operates without any free parameters. However, the cosmic web classification technique involves two parameters: the smoothing length $R_{\rm s}$ and the threshold $\lambda_{\rm th}$, both of which can influence the filament catalogue derived from the dark-matter particle density distribution (Zhang et al. 2024). In the following analysis, we focus primarily on the findings for $\lambda_{\rm th} = 0.2$ and 0.8, using the smoothing lengths of $R_{\rm s} = 2.1\,h^{-1}$Mpc and $4.0\,h^{-1}$Mpc.

Fig. 1 demonstrates that by increasing $R_{\rm s}$ or $\lambda_{\rm th}$, the filament detection method effectively eliminates a large number of less significant filaments (see also figs 1 and 2 in Zhang et al. 2024).

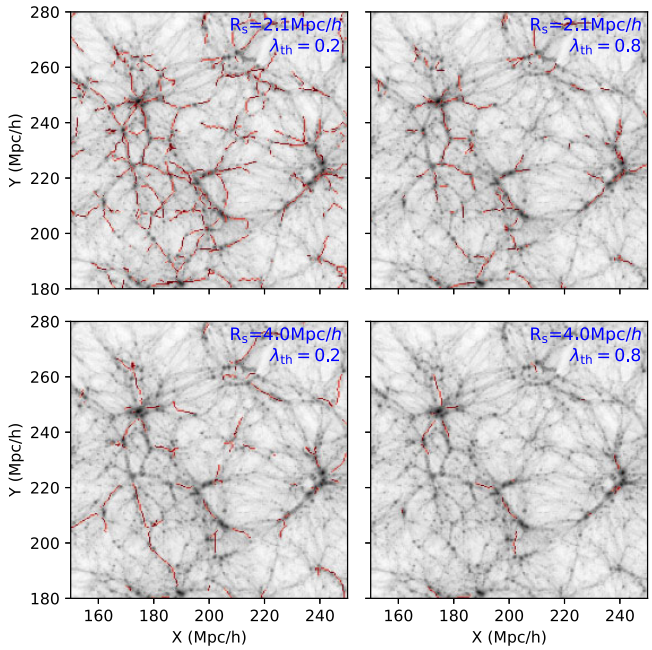

Figure 1. Distribution of density (black) and filament axes (red) within a $10\,h^{-1}$Mpc wide slice from the ELUCID simulation. The COWS technique is employed to identify the filament axes, utilizing cosmic web classifications based on varying values of R_s and λ_{th}.

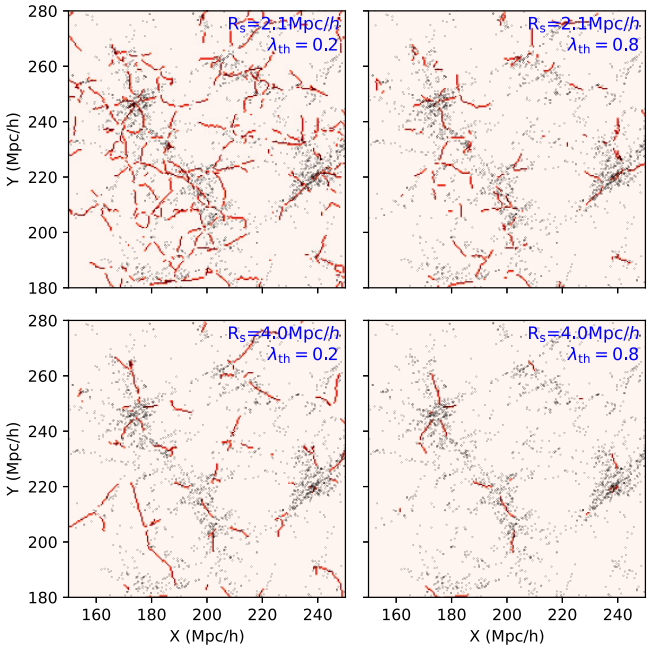

Figure 2. Similar to Fig. 1, but for the COWS filaments overlaid on the galaxy distribution from SDSS DR7.

In the filament catalogue, for $R_s = 2.1\,h^{-1}$Mpc and $\lambda_{th} = 0.2$ in the SDSS area, there are 390 001 filament segments. In comparison, for $R_s = 4.0\,h^{-1}$Mpc and $\lambda_{th} = 0.8$, the catalogue records 27 978 segments. An increase in R_s or λ_{th} results in a reduction in filaments. It is assumed that the spines of the filaments run through the centres of the filament cells. A filament consists of several segments, each segment connecting the centres of adjacent cells along the filament.

This research examines the properties of galaxies/haloes around the segments that make up the filament.

It is well established that the eigenvectors $\hat{\boldsymbol{e}}_3$ serve as indicators for the directions of the filaments in numerous studies (Zhang et al. 2009, 2013, 2015). According to Zhang et al. (2024), we confirmed that the filament axes identified by the COWS method align well with the eigenvector $\hat{\boldsymbol{e}}_3$ of the Hessian matrix of the smoothed density field, regardless of the various parameters R_s and λ_{th}. This validates the effectiveness of the COWS method. Zhang et al. (2024) observed that the probability distribution function for the filament lengths relies solely on the smoothing length R_s and remains largely consistent across various λ_{th} thresholds. Furthermore, this study reveals that the characteristics analysed concerning their distance from the filament spines show similar increasing or decreasing trends across various parameters R_s and λ_{th}. However, the observed trend of decreasing or increasing is relatively weak in the catalogue of filaments characterized by $R_s = 2.1\,h^{-1}$Mpc and $\lambda_{th} = 0.2$.

3 RESULTS

This section explores the variation in galaxy and halo properties in relation to their distance to filament axes, determined using the medial-axis thinning algorithm as employed in the COWS technique. The attributes of galaxies under investigation include stellar mass, colour, sSFR, size, and the elliptical-to-spiral ratio (E/S ratio). For haloes, the characteristics evaluated encompass mass, age, radius, spin, and concentration.

3.1 Galaxies properties in observation

3.1.1 Stellar mass

The filament catalogues used in this research are derived from the distribution of dark matter particles within the ELUCID simulation.

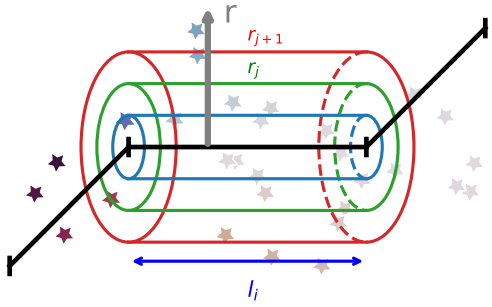

Figure 3. Illustration of segment i with length l_i, useful for determining averaged values in the jth shell, characterized by a thickness of $r_{j+1} - r_j$. The radial distance from the axis of the filament is represented by r. In this study, each cylindrical segment i is divided into 10 cylindrical shells.

This simulation replicates the cosmic web structure found in SDSS, as its initial conditions are based on the density field observed in the SDSS data (Wang et al. 2014). We assessed the stellar mass close to the axes of filaments as determined in the ELUCID simulation, using the distribution of galaxies, with their observed positions mapped into the ELUCID simulation's coordinate system.

In the algorithm for detecting filaments, the cosmic web environment is categorized for 1024^3 cells within a $500\,h^{-1}$Mpc box. The filament axes are considered to traverse the centre of each filament cell. However, their precise locations within a $0.5\,h^{-1}$Mpc cell remain uncertain. Therefore, to exclude the core region where the positions of the filament axes are ambiguous, this study sets the minimum profile radius at $0.5\,h^{-1}$Mpc. The filament catalogue produced using the COWS method defines a filament as being composed of multiple linked segments. In our study, we analyse the distribution of stellar mass around each segment of these filaments. Each cylindrical segment is divided into 10 cylindrical shells, employing uniform logarithmic bins centred along the axis. These bins extend from an inner radius of $r = 0.5\,h^{-1}$Mpc to $r = 20\,h^{-1}$Mpc for each segment. We then calculated the average stellar mass values of galaxies within each radial shell for all segments listed in the catalogue. A filament is made up of several interconnected segments. As illustrated in Fig. 3, the average stellar mass for the jth cylindrical shell, with a thickness of $r_{j+1} - r_j$, is determined by summing the stellar masses of all galaxies within this shell and dividing by the total count of galaxies across all segments.

Fig. 4 illustrates the stellar mass of galaxies from SDSS DR7 in relation to their distance to the filament spines, identified via the COWS method. The different lines represent the average values for the respective scenarios R_s and $\lambda_{\rm th}$. The error bars in Fig. 4 are obtained by bootstrapping segment profiles using the `astropy.stats.bootstrap` function from the `Astropy` library.[4] A random subset of segments is repeatedly selected from the complete set, and the averages of these selections are calculated. The random sampling and averaging procedure is carried out 100 times to generate 100 mean estimates. From these means, the standard error is calculated to create the error bars shown in Fig. 4.

Overall, as illustrated in Fig. 4, galaxies tend to show a growth in stellar mass as they approach filaments, which is consistent with results from previous observations (Chen et al. 2017; Malavasi et al. 2017; Hoosain et al. 2024). As described in Section 2.3, the approach for determining filaments involves two key parameters:

[4]http://www.astropy.org

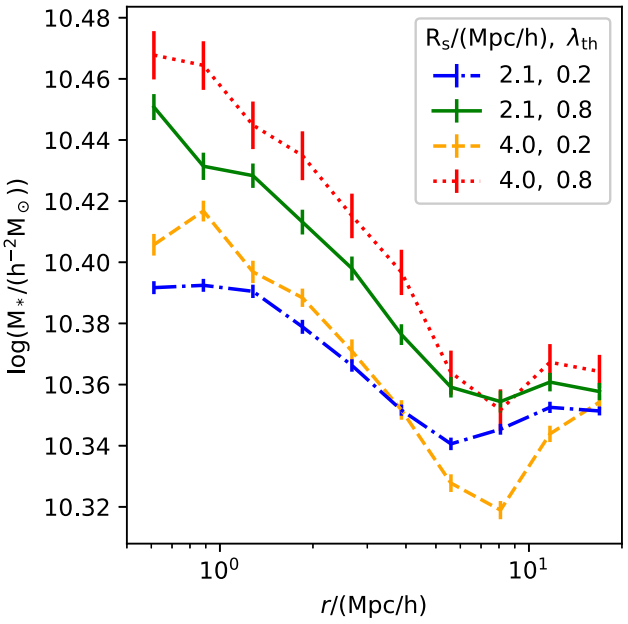

Figure 4. Stellar mass of galaxies from SDSS DR7 as a function of their distance to the filament spines identified by the COWS method, using varying parameters for $R_{\rm s}$ and $\lambda_{\rm th}$. The average values of stellar mass are calculated in shells around filaments, illustrated by the different line types, indicating the average stellar mass decreases with the distance to filament axes. The error bars are derived from 100 bootstrap samples.

the smoothing length, $R_{\rm s}$, and the threshold, $\lambda_{\rm th}$, both influencing the filament catalogue derived from the dark-matter particle distribution. It is worth exploring how galaxy properties near filaments are affected by these parameters. Fig. 4 illustrates how stellar masses are distributed among galaxies close to the filament under four conditions: $R_s = 2.1,\ 4.0\,h^{-1}$Mpc, and $\lambda_{\rm th} = 0.2,\ 0.8$.

Fig. 4 illustrates that with higher values of $R_{\rm s}$ and $\lambda_{\rm th}$, the increase in stellar mass is more pronounced as galaxies approach filaments. This pattern is especially noticeable in the filament catalogue when using the parameters $R_{\rm s} = 4.0\,h^{-1}$Mpc and $\lambda_{\rm th} = 0.8$, as this configuration retains only the most significant filaments. In the previous study by Zhang et al. (2024), we analysed the statistical properties of the filaments using different parameters $R_{\rm s}$ and $\lambda_{\rm th}$. We confirmed that the filaments increase both in length and in thickness as $R_{\rm s}$ increases. As the smoothing length $R_{\rm s}$ increases, less prominent filaments are typically omitted from the filament catalogue, which enhances the observed trend of increasing mass closer to filaments for $R_{\rm s} = 4.0\,h^{-1}$Mpc and $\lambda_{\rm th} = 0.8$.

3.1.2 *Galaxy colour*

The colour of a galaxy offers valuable information about its SFR, quenching mechanisms, and the age of its stellar population. In the following analysis, we examine how changes in galaxy colour relate to different distances from the centres of filaments.

As mentioned in Section 3.1.1, the mass of the galaxy is significantly influenced by its proximity to filament axes. To reduce the influence of stellar mass on our findings, we classify galaxies into three separate mass categories specified by $\log(M_*/(\,h^{-2}{\rm M}_\odot))$: (9,10), (10,10.5), and (10.5,11.5). These categories contain 129 651, 195 540, and 176 551 galaxies, respectively.

Fig. 5 illustrates how galaxy colours ${}^{0.1}(g-r)$ vary with the distance to the filament spines determined using the COWS method,

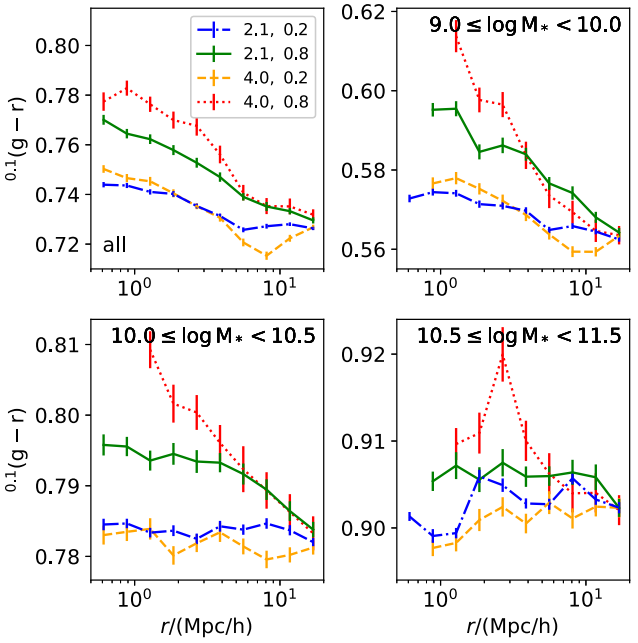

Figure 5. Galaxy colours as a function of the distance to the filament spines identified by the COWS method, employing different parameters for $R_s = 2.1, 4.0\,h^{-1}$Mpc and $\lambda_{th} = 0.2, 0.8$. The top-left panel presents the findings for all galaxies in the sample, while the other panels depict results divided by galaxy mass bins with $\log(M_*/(\,h^{-2}\mathrm{M}_\odot))$ spanning (9,10), (10,10.5), and (10.5,11.5), respectively.

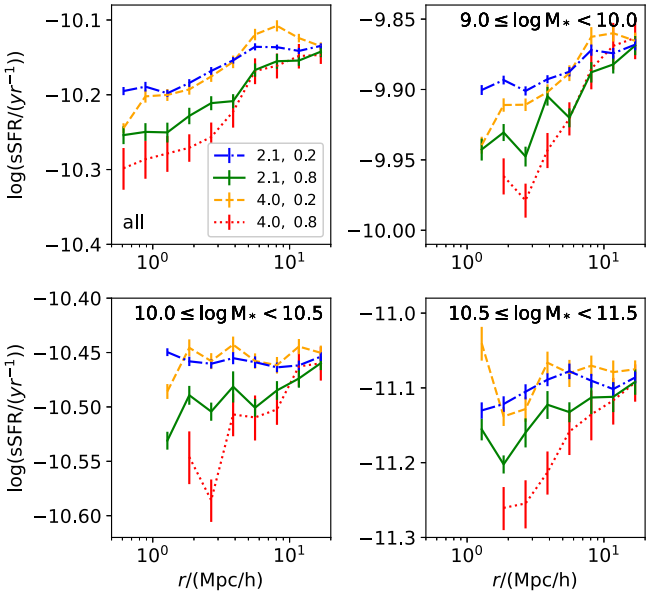

Figure 6. SSFR as a function of the distance to the filament spines identified by the COWS method, using varying parameters for $R_s = 2.1, 4.0\,h^{-1}$Mpc and $\lambda_{th} = 0.2, 0.8$. The top-left panel shows the results for the entire galaxy sample, whereas the remaining panels display findings segmented by galaxy mass categories with $\log(M_*/(\,h^{-2}\mathrm{M}_\odot))$ ranges of (9,10), (10,10.5), and (10.5,11.5), respectively.

with parameters set at $R_s = 2.1, 4.0\,h^{-1}$Mpc and $\lambda_{th} = 0.2, 0.8$. In Fig. 5, the top-left panel illustrates the results for the entire galaxy sample with a mass of $\log(M_*/(\,h^{-2}\mathrm{M}_\odot)) \geq 9.0$. The remaining panels show results segmented by galaxy mass bins with $\log(M_*/(\,h^{-2}\mathrm{M}_\odot))$ intervals of (9,10), (10,10.5), and (10.5,11.5), respectively. Overall, galaxies exhibit a redder colour as they approach the cores of filaments, consistent with earlier research (Kraljic et al. 2018; Tugay & Tarnopolski 2023). Furthermore, the change in colour with respect to the distance to the filament spines is more evident with larger R_s or λ_{th}.

As depicted in Fig. 5, within a particular range of stellar masses, galaxies are also redder when they are located close to filaments, especially at $R_s = 4.0\,h^{-1}$Mpc and $\lambda_{th} = 0.8$. However, the correlation between galaxy colours and their distance to filament axes is quite weak for $R_s = 2.1\,h^{-1}$Mpc and $\lambda_{th} = 0.2$.

Galaxies in dense filament environments experience gas stripping, tidal interactions, and quenching mechanisms (e.g. ram-pressure stripping, strangulation), which suppress star formation and lead to older, redder stellar populations. These processes are most efficient in the high-density cores of well-defined filaments (Bulichi et al. 2024). A more pronounced correlation between galaxy colour and proximity to filament spines at higher R_s or λ_{th} probably arises from improved detection of prominent filaments. An increased R_s leads to a smoothing of the cosmic density field over more extensive scales, thereby averaging out the noise on smaller scales and more effectively revealing the actual geometry of the filaments. For example, at $R_s = 4.0\,h^{-1}$Mpc, noise-induced 'fake' filaments in low-density regions are smoothed away, leaving only robust filaments. In well-defined filaments, processes like ram-pressure stripping and tidal interactions efficiently suppress star formation, leading to redder galaxies near filaments.

3.1.3 Specific star formation rate

As indicated by Winkel et al. (2021), a study using the SDSS survey demonstrated that galaxies show increased sSFRs as their separation from cosmic web filaments grows, using a filament catalogue created with the DisPerSE approach. In this research, we investigate how the sSFR varies in relation to the separation from the filaments, employing a catalogue formulated using the COWS methodology. The sSFRs for galaxies in our analysis are sourced from the publicly accessible catalogue by Chang et al. (2015), which offers reliable aperture corrections.

Fig. 6 shows how the sSFR varies with the distance to the filament spines, as determined by the COWS approach. The upper left panel illustrates an increase in the sSFR of the whole sample as the distance from the filament spines grows. This aligns with the results reported in the filament catalogues obtained using the DisPerSE method (Laigle et al. 2018; Luber et al. 2019; Bonjean et al. 2020; Winkel et al. 2021). As shown by the green line at $R_s = 2.1\,h^{-1}$Mpc and $\lambda_{th} = 0.8$ in Fig. 6, a consistent trend is evident across specified mass intervals $\log(M_*/(\,h^{-2}\mathrm{M}_\odot))$, including (9,10), (10,10.5), and (10.5,11.5). Moreover, the variation in sSFR in relation to the proximity to filament spines becomes more pronounced with higher R_s or λ_{th} values. This trend is particularly significant for $R_s = 4.0\,h^{-1}$Mpc and $\lambda_{th} = 0.8$.

The more pronounced trend of sSFR in $R_s = 4.0\,h^{-1}$Mpc and $\lambda_{th} = 0.8$ arises from the interaction of environmental quenching and improved filament identification. $R_s = 4.0\,h^{-1}$Mpc smooths the density field across more extensive scales, thus eliminating minor fluctuations and highlighting significant filaments. These filaments maintain dynamic stability, while environmental influences, such as ram-pressure stripping and tidal stripping, act effectively. In these well-defined filaments, galaxies located close to spines are subjected to extended periods of quenching processes. Briefly, increasing R_s or λ_{th} better traces physically realistic filaments where environmen-

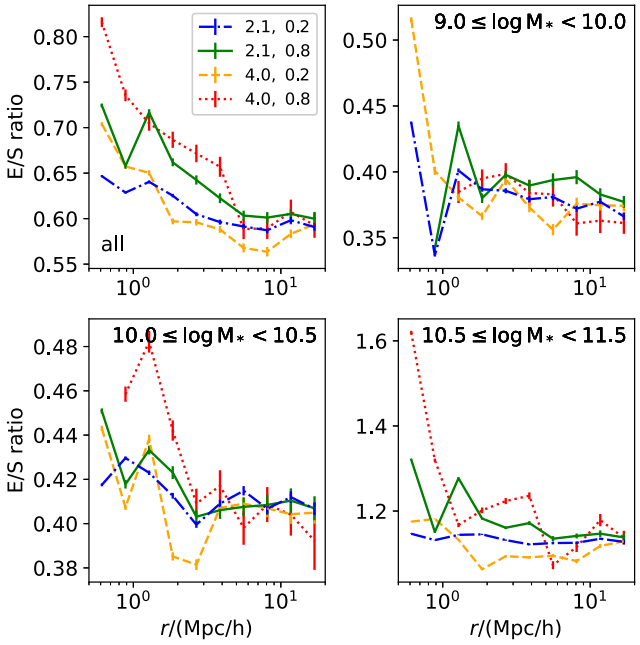

Figure 7. Ratios of elliptical to spiral galaxy counts as a function of the distance to the filament spines identified by the COWS method, using varying parameters for $R_s = 2.1, 4.0\,h^{-1}$Mpc and $\lambda_{\rm th} = 0.2, 0.8$. The top-left panel shows the results for the entire galaxy sample, whereas the remaining panels display findings segmented by galaxy mass categories with $\log(M_*/(\,h^{-2}{\rm M}_\odot))$ ranges of (9,10), (10,10.5), and (10.5,11.5), respectively.

tal impacts are more significant, thus strengthening the observed correlation with the decrease in sSFR around these filaments.

3.1.4 Galaxy morphology

The GZ2 catalogue (Willett et al. 2013) serves as the basis for categorizing galaxies into elliptical and spiral types. Using this catalogue, we have identified 107 230 elliptical galaxies and 134 024 spiral galaxies in our NYU-VAGC data set.

The top-left panel of Fig. 7 presents an illustration showing the ratio of elliptical to spiral galaxy counts (E/S ratio) as a function of their distance from filaments, determined using the COWS method throughout the entire galaxy data set. The remaining panels further detail these findings by galaxy mass with $\log(M_*/(\,h^{-2}{\rm M}_\odot))$ defined as intervals of (9,10), (10,10.5), and (10.5,11.5), respectively. For the whole galaxy sample, the E/S ratio tends to increase near the filament spines. The trends of the E/S ratio depicted in Fig. 7 vary based on the parameters R_s, $\lambda_{\rm th}$, and the mass of the galaxy. Galaxies in filaments for $R_s = 4.0\,h^{-1}$Mpc and $\lambda_{\rm th} = 0.8$ show a pronounced increase in the E/S ratio towards their spines, particularly for high-mass galaxies ($\log(M_*/(\,h^{-2}{\rm M}_\odot)) \geq 10.5$), consistent with dense filament environments driving morphological quenching. In contrast, trends are weaker or absent for filaments with $R_s = 2.1\,h^{-1}$Mpc and $\lambda_{\rm th} = 0.2$ and low-mass galaxies ($\log(M_*/(\,h^{-2}{\rm M}_\odot)) < 10.0$), where environmental effects are less influential. The flat trends observed in these subsets probably indicate that less prominent filaments do not possess sufficient gravitational and thermal energy to strip the gas effectively, resulting in weaker morphological trends. Additionally, low-mass galaxies retain gas reservoirs longer, buffering them against environmental effects. This results in minimal morphological transformation, even near dense filaments.

This result, an increase in the E/S ratio towards filament spines, is qualitatively consistent with the trends reported by Kuutma et al. (2017) and O'Kane et al. (2024), although these studies differ in their interpretation of the role of local density. Kuutma et al. (2017) found persistent morphological trends near filaments identified using the Bisous model even after controlling for local density, whereas O'Kane et al. (2024) reported that the trends vanished for DisPerSE-based filaments when accounting for density. Our results contribute to the growing evidence that filaments influence galaxy morphology while underscoring the need for future studies to jointly model filament geometry and local density.

3.1.5 Galaxy size in observation

The sizes of galaxies are a crucial observational characteristic essential for refining models of how galaxies evolve. Many studies have examined the relationship between galaxy size and stellar mass (Zhang & Yang 2019), as well as the scaling relation connecting galaxies to dark-matter haloes (Zhang et al. 2022). The established scaling relations between galaxy sizes and stellar masses (e.g. the mass–size relation) show significant scatter in dense environments. By correlating size residuals with filament distance, we can disentangle the roles of internal (e.g. stellar feedback) versus external (e.g. filament-driven accretion) processes in shaping these relations, offering a pathway to refine semi-analytic models. It is intriguing to explore how the size of galaxies is influenced by the large-scale cosmic environment. Furthermore, it is intriguing to explore how the size of galaxies is influenced by the large-scale cosmic environment. Consequently, this section investigates the connection between a galaxy's size and its distance to cosmic filaments.

This research employs half-light radii R_{50} of galaxies obtained from the NYU-VAGC catalogue. As reported by Zhang et al. (2022), the galaxy sizes in the NYU-VAGC catalogue are consistent with those found in the catalogues of Simard et al. (2011) and Meert et al. (2015) for galaxies with similar stellar masses.

Fig. 8 shows how the galaxy size R_{50} correlates with their proximity to the axes of filaments, identified using the COWS technique in various mass ranges: $\log(M_*/(\,h^{-2}{\rm M}_\odot))$, including (9,10), (10,10.5), and (10.5,11.5). In the mass intervals of (9,10) or (10,10.5), galaxies generally exhibit smaller sizes near the filament spines. On the other hand, in the (10.5,11.5) mass range, galaxies tend to increase in size as they get closer to the filament axes. A potential reason is that, as low-mass galaxies are pulled into filaments, they tend to become more compact due to tidal stripping. The reduced size of low-mass galaxies near filaments aligns with tidal stripping processes, where galaxies entering dense filamentary environments lose their outer stellar and dark-matter components due to gravitational interactions with neighbouring structures. In contrast, high-mass galaxies generally grow in size, primarily as a result of minor mergers (Naab, Johansson & Ostriker 2009) or active galactic nucleus (AGN)-driven winds (Cochrane et al. 2023), which are more common in proximity to filaments. High-mass galaxies near filaments often host AGNs. Filament-fed gas inflows trigger AGN activity, generating powerful winds that expel gas from the galactic centre. This feedback suppresses central star formation while redistributing gas to the outer disc, leading to disc expansion.

Analysing galaxies from the LOWZ sample in SDSS DR12, Chen et al. (2017) investigated how galaxy size correlates with their distance to cosmic filaments, focussing on galaxies with masses within the range $11.5 \leq \log(M_*/M_\odot) < 12$. Their findings suggest that smaller galaxies generally have greater mean distances

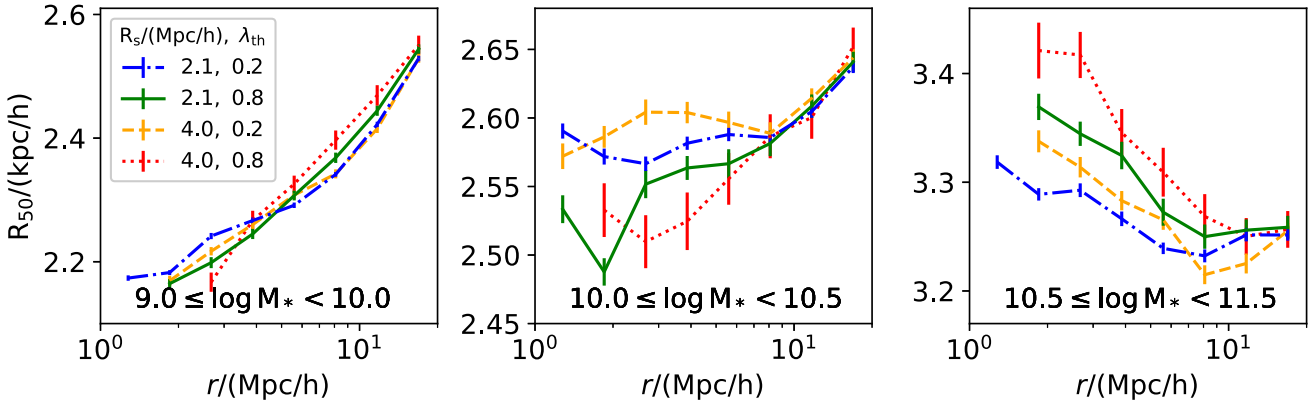

Figure 8. Galaxy half-light radii R_{50} as a function of distances from filament spines, identified with the COWS technique for $R_s = 2.1, 4.0\,h^{-1}$Mpc and $\lambda_{th} = 0.2, 0.8$, over different mass intervals of $\log(M_*/(h^{-2}\mathrm{M}_\odot))$ such as (9,10), (10,10.5), and (10.5,11.5).

from filaments, consistent with the patterns observed for high-mass galaxies ($\log(M_*/(h^{-2}\mathrm{M}_\odot)) > 10.5$) in this analysis.

3.2 Halo properties in simulation

3.2.1 Subhalo mass

In the ELUCID simulation, the SUBFIND algorithm (Springel et al. 2001) is applied to divide a parent FOF halo into several gravitationally bound subhaloes. The largest of these is identified as the central subhalo, and the others are known as satellite subhaloes. To obtain a more precise determination of halo properties such as radius, formation time, spin, and concentration, it is beneficial to use a greater number of particles in larger haloes compared to smaller ones with fewer particles. Therefore, we mainly focus on central subhaloes with a mass M_h greater than $10^{11}\,h^{-1}\mathrm{M}_\odot$ and containing at least 300 dark matter particles.

The mass of the central subhalo, denoted as M_h, is very close to the virial mass M_{vir} of its host halo. The virial mass is calculated as the total mass within a spherical radius R_{vir}, centred on the particle with the lowest potential energy. In the ELUCID simulation, the proportion of M_h to M_{vir} for the central subhaloes is determined to be 1.02 ± 0.08. In the following analysis, unless otherwise stated, the central subhalo mass M_h will be used in this study.

Fig. 9 presents the masses of the central subhaloes in the ELUCID simulation, plotted against their distances from the filament spines identified by the COWS method, with varying parameters for R_s and λ_{th}. For $R_s = 4.0\,h^{-1}$Mpc, the masses of central subhaloes tend to decrease as the distance to the nearest filament increases, aligning with the observed pattern that more massive galaxies are situated near filaments.

For $R_s = 2.1\,h^{-1}$Mpc, the subhalo mass decreases with increasing radial distance r, reaching its minimum at approximately twice the smoothing length. Previous studies (Pfeifer et al. 2022; Yang, Hudson & Afshordi 2022; Zhang et al. 2024) have discovered a valley in the density profiles of filaments. Similarly to these density profiles, the observed valley in halo mass in the vicinity of filaments may stem from the use of the CIC interpolation method within the COWS approach to create the density field with $R_s = 2.1\,h^{-1}$Mpc. For further details, see section 3.4 in Zhang et al. (2024).

3.2.2 Subhalo formation time

In the ELUCID simulation, merger trees are formed by connecting subhaloes that are detected using the SUBFIND algorithm. The

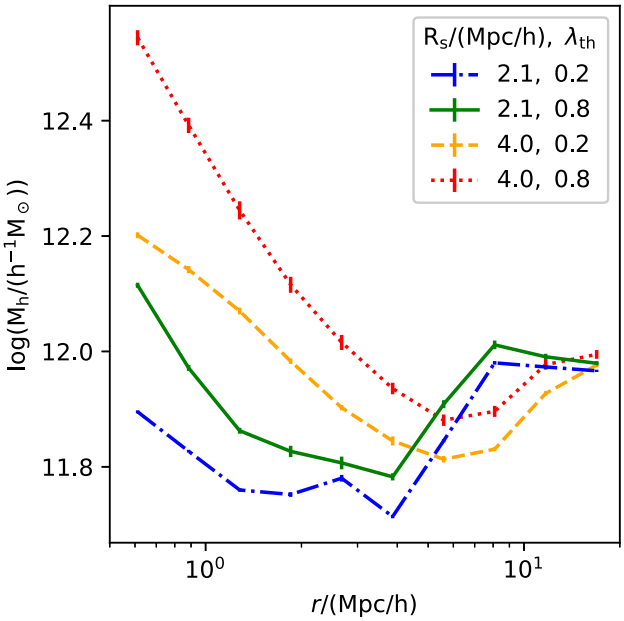

Figure 9. Subhalo mass from the ELUCID simulation in relation to their distances from filament spines determined by the COWS technique, using different settings for R_s and λ_{th}.

formation redshift of a subhalo, denoted as z_f, is characterized as the redshift where the main branch progenitor attained half of its maximum mass. To achieve an accurate estimate of the subhalo formation time, our primary focus is on subhaloes comprising a minimum of 300 dark-matter particles, each having a mass greater than $10^{11}\,h^{-1}\mathrm{M}_\odot$.

Fig. 10 illustrates the redshift at which central subhaloes form, z_f, as a function of their distances from the cores of filaments, which are identified using the COWS method with parameter values $R_s = 2.1, 4.0\,h^{-1}$Mpc and $\lambda_{th} = 0.2, 0.8$. The top-left panel of Fig. 10 illustrates that for the entire sample of 3324 498 central subhaloes with $M_h \geq 10^{11}\,h^{-1}\mathrm{M}_\odot$, the formation redshifts generally decrease with increasing distance to the filament spines.

To reduce the impact of the subhalo mass on our results, we divide the subhaloes into three distinct mass ranges defined by $\log(M_h/(h^{-1}\mathrm{M}_\odot))$: (11,11.5), (11.5,12), and (12,13). These ranges encompass 2171 045, 759 136, and 354 741 subhaloes, respectively. As depicted in Fig. 10, within a specific subhalo mass range,

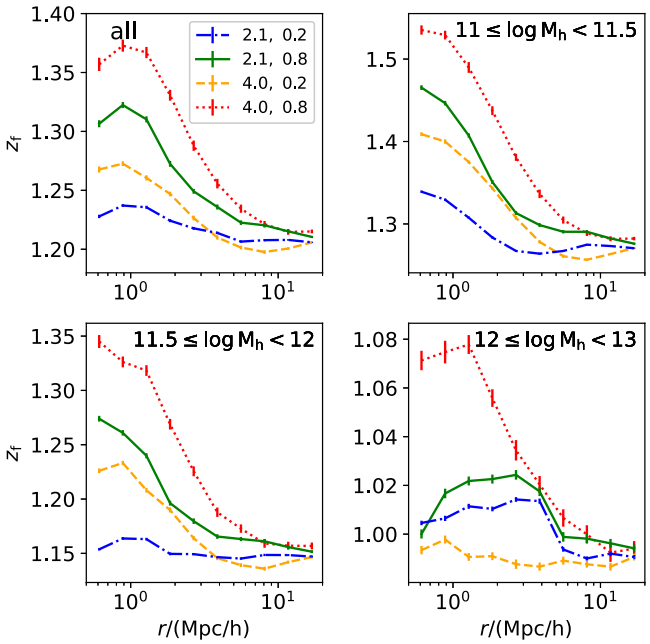

Figure 10. Subhalo formation redshift $z_{\rm f}$ as a function of their distance to the filament spines, identified through the COWS method using parameters $R_{\rm s} = 2.1, 4.0\,h^{-1}$Mpc and $\lambda_{\rm th} = 0.2, 0.8$. The top-left panel presents results from our data set of all central subhaloes with masses greater than $10^{11}\,h^{-1}{\rm M}_{\odot}$. The other panels show data segregated by subhalo mass ranges for $\log(M_{\rm h}/(\,h^{-1}{\rm M}_{\odot}))$, specifically within (11,11.5), (11.5,12), and (12,13).

the subhaloes located near the filament spines tend to be older, particularly for $R_s = 4.0\,h^{-1}$Mpc and $\lambda_{\rm th} = 0.8$. The correlation between halo formation redshifts and their proximity to filaments is consistent with patterns noted in galaxies. This is anticipated because galaxies exhibiting redder colours and reduced sSFRs tend to be located closer to filaments.

3.2.3 Halo size in simulation

This study uses ELUCID simulation to investigate how halo radii, particularly $R_{1/2}$ and $R_{\rm vir}$, vary in relation to their proximity to filament spines. The radius $R_{\rm vir}$ represents the boundary where the mean density of dark-matter haloes is $\Delta_{\rm vir}$ times the universe's critical density (Bryan & Norman 1998). The radius $R_{1/2}$ is characterized as the radius enclosing half of the halo's mass $M_{\rm h}$, where $M_{\rm h} = 1.02 \pm 0.08 M_{\rm vir}$ according to the ELUCID simulation framework.

Fig. 11 shows how the halo radii $R_{1/2}$ and $R_{\rm vir}$ vary with the distance to the filament spines identified by the COWS method, considering various parameters such as $R_{\rm s} = 2.1, 4.0\,h^{-1}$Mpc and $\lambda_{\rm th} = 0.2, 0.8$, in the mass ranges of $\log(M_{\rm h}/\,h^{-1}{\rm M}_{\odot})$ between (11,11.5), (11.5,12), and (12,13). The lower panels of Fig. 11 illustrate that the virial radii $R_{\rm vir}$ decrease as the distance to the filament spines increases. In contrast, the upper panels show that for low-mass haloes of $11.0 \leq \log(M_{\rm h}/\,h^{-1}{\rm M}_{\odot}) < 11.5$, the half-mass radii $R_{1/2}$ increase with increasing distance to the filament spines, particularly for $R_{\rm s} = 4.0\,h^{-1}$Mpc.

For low-mass haloes, the decrease in their half-mass radii $R_{1/2}$ near filaments is similar to the pattern noted in the half-light radii R_{50} of low-mass galaxies with masses in the range $(9.0 \leq \log(M_*/(\,h^{-2}{\rm M}_{\odot})) < 10.0)$. This is driven by tidal compression and stripping in dense filamentary environments. Filament spines generate strong tidal forces that strip loosely bound outer material, truncating haloes and compacting their mass distribution. This process preferentially removes dark matter from the outskirts of the halo, reducing $R_{1/2}$ while preserving the core mass. Generally, tidal stripping affects both dark-matter haloes and their embedded galaxies, suppressing gas reservoirs and star formation in galaxies, leading to compact stellar distributions.

For high-mass haloes, the variation in $R_{1/2}$ in proximity to filaments aligns with the alteration in $R_{\rm vir}$ around filaments. Massive haloes situated near cosmic filaments primarily expand via mergers and the inflow of gas channelled through the cosmic web, similar to how high-mass galaxies increase in size through mergers. This process of mass accumulation contributes mainly to the outer regions of the halo, resulting in a concurrent expansion of both $R_{\rm vir}$ and $R_{1/2}$.

3.3 Halo concentration and spin

This section investigates how halo concentration and spin vary in relation to their distance to filament spines, based on data obtained from the ELUCID simulation.

The concentration values $c_{\rm vir}$ are derived from dark matter haloes based on the ELUCID simulation, as described in equation (5). Fig. 12 presents the variation of the halo concentration $c_{\rm vir}$ relative to the proximity to the filament cores, determined using the COWS method with different settings for $R_{\rm s} = 2.1, 4.0\,h^{-1}$Mpc and $\lambda_{\rm th} = 0.2, 0.8$. In general, as the haloes approach the filaments, their concentration increases, particularly when $R_{\rm s} = 4.0\,h^{-1}$Mpc and $\lambda_{\rm th} = 0.8$. However, this pattern is not observed for $R_{\rm s} = 2.1\,h^{-1}$Mpc and $\lambda_{\rm th} = 0.2$.

Using two distinct collections of cosmological hydrodynamical simulations, Jiang et al. (2019) demonstrated that the ratio of the size of a galaxy to the virial radius of the halo is expressed as $c_{\rm vir}^{-0.7}$. This result suggests an inverse correlation between galaxy size and halo concentration. In the case of galaxies that reside in low-mass haloes, an increase in halo concentration close to filaments could lead to

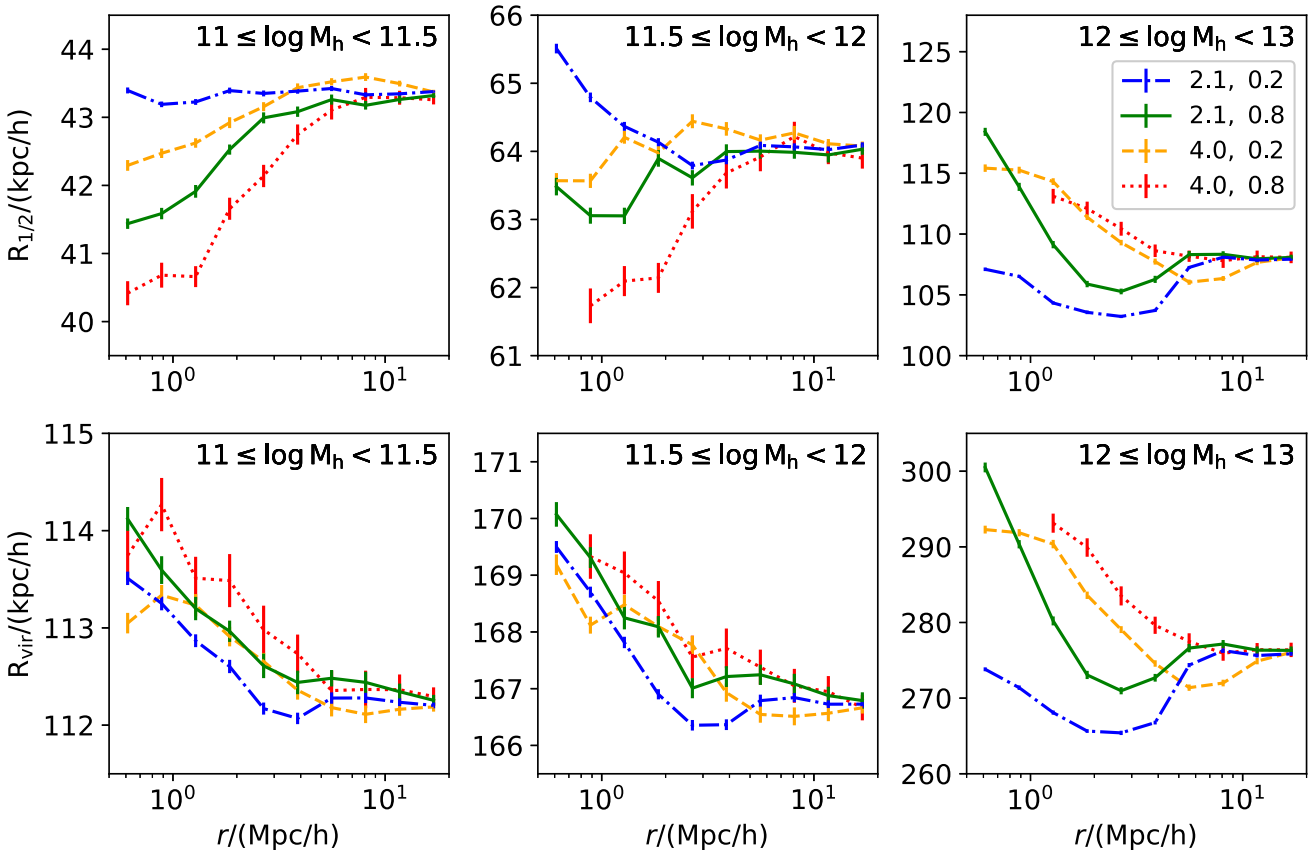

Figure 11. Halo radii as a function of the distance to the filament spines that are identified via the COWS method, utilizing different parameters including $R_s = 2.1, 4.0\,h^{-1}$Mpc and $\lambda_{th} = 0.2, 0.8$, across the mass ranges of $\log(M_h/\,h^{-1}M_\odot)$ of (11,11.5), (11.5,12), and (12,13). The upper panels show the outcomes for the half-mass radius, whereas the lower panels exhibit the results for the halo virial radius.

reduced sizes of such low-mass galaxies near these filaments. For galaxies in high-mass haloes, galaxy mergers may be the main driver of the size evolution (Khochfar & Silk 2006; Cooper et al. 2012; Figueira et al. 2024).

In this study, the spin values λ are derived from equation (4) with the use of subhaloes within the ELUCID simulation. Fig. 13 depicts the halo spin parameter λ as a function of the distance to the filament spines determined using the COWS method, using varying settings for $R_s = 2.1, 4.0\,h^{-1}$Mpc and $\lambda_{th} = 0.2, 0.8$. The upper left panel presents data from our collection of all central subhaloes with masses greater than $10^{11}\,h^{-1}M_\odot$. The other panels illustrate data segmented by subhalo mass ranges for $\log(M_h/(\,h^{-1}M_\odot))$, covering the intervals (11,11.5), (11.5,12), and (12,13).

In general, as the distance to the filament axes increases, the spin values tend to decrease. This pattern is consistent with the findings of Xue, Rong & Hua (2024), who analysed the rotational speeds of haloes by studying H I gas-rich galaxies observed in the Arecibo Legacy Fast Alfa Survey. Their research revealed that haloes with higher spin values tend to be situated nearer to filaments.

The tendency of high-spin haloes to reside near filaments arises from the interplay between filament-driven angular momentum transfer and anisotropic mass accretion.

During the stages of structure formation, haloes acquire angular momentum through tidal torquing, where misalignments between the halo inertia tensor and the local tidal field generate spin. Filaments are regions of high tidal shear due to their elongated geometry and dense matter distribution. This amplifies the tidal torque, increasing the acquisition of angular momentum compared to isotropic environments.

Filaments channel gas and dark matter flows preferentially along their axes, driving coherent accretion on to haloes. Gas streaming along filaments retains the angular momentum of large-scale flows, which is transferred to haloes during accretion. While major mergers randomize the spin of the halo, minor mergers, which dominate in filament environments, can amplify the spin. Minor mergers along filaments deliver satellites with aligned trajectories, transferring orbital angular momentum to the spin of the halo.

Generally, filaments act as cosmic highways for angular momentum, channelling coherent flows that spin up haloes through tidal torquing, anisotropic accretion, and minor mergers. This explains the observed spin-distance trend and aligns with the Lambda cold dark matter predictions of the web-regulated galaxy–halo evolution.

4 SUMMARY

In this study, we examine the properties of galaxies and haloes in terms of their distance to cosmic filaments, using galaxies from SDSS DR7 and haloes in the constrained ELUCID simulation. The characteristics of galaxies that are being analysed encompass stellar mass, colour, sSFR, size, and the E/S ratio. In terms of haloes, our study focuses on attributes such as mass, age, radius, spin, and concentration.

The structure of the cosmic web, which consists of knots, filaments, sheets, and voids, is classified through the Hessian matrix

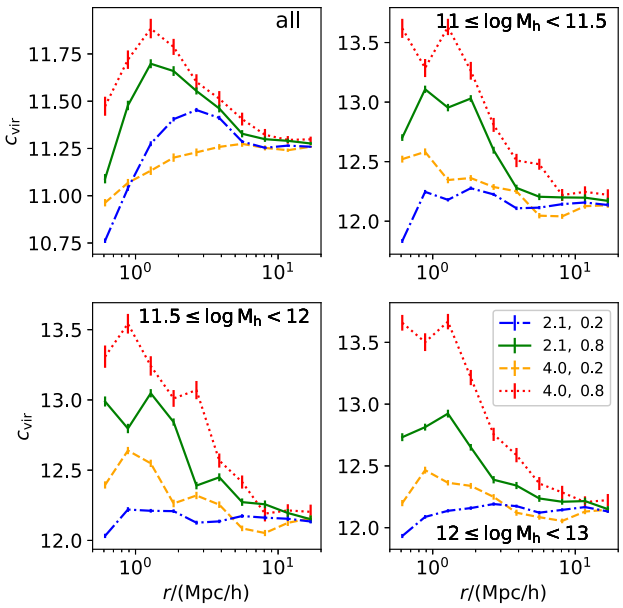

Figure 12. Halo concentration $c_{\rm vir}$ as a function of the distance to the filament spines identified by the COWS method, employing different parameters for $R_{\rm s} = 2.1, 4.0\,h^{-1}$Mpc and $\lambda_{\rm th} = 0.2, 0.8$. The top-left panel illustrates data from our sample of all central subhaloes with masses exceeding $10^{11}\,h^{-1}{\rm M}_{\odot}$. The remaining panels display data categorized by subhalo mass brackets for $\log(M_{\rm h}/(\,h^{-1}{\rm M}_{\odot}))$, specifically within the intervals (11,11.5), (11.5,12), and (12,13).

related to the density field, as detailed in equation (7). In order to examine the properties of galaxies or haloes surrounding filaments, the filament axes are determined using the medial axis thinning technique implemented in the COWS method (Pfeifer et al. 2022). As illustrated in Fig. 1, the medial axes effectively outline the spines of cosmic filaments, which are prominently shaped by the arrangement of dark matter particles. Our validation process confirmed that the filament axes obtained using the medial axis thinning technique are well aligned with the eigenvector of the Hessian matrix corresponding to the orientation of the filament, thus supporting the filament axes identification method (Zhang et al. 2024).

Although the medial-axis thinning algorithm operates without any adjustable parameters, the method to classify the cosmic web depends on two specific variables: the smoothing length $R_{\rm s}$ and the threshold $\lambda_{\rm th}$. We verified our results with several filament catalogues using different values of $R_{\rm s}$ or $\lambda_{\rm th}$, and in most cases, the main conclusions are consistent in various parameters.

However, filaments with reduced lengths and thinner shapes, specified by parameters $R_{\rm s} = 2.1\,h^{-1}$Mpc, $\lambda_{\rm th} = 0.2$, show a weak trend of increase or decrease, as represented by the blue dot–dashed lines. The weak increase or decrease in the tread for $R_{\rm s} = 2.1\,h^{-1}$Mpc, $\lambda_{\rm th} = 0.2$ resembles the density reconstruction impact as described in Hasan et al. (2024), where the use of DTFE density reconstruction to study galaxies indicates a decrease in star formation in galaxies near filaments. In contrast, filaments identified using the MCPM method appear to exert minimal impact on star formation activities.

As noted in Hasan et al. (2024), the MCPM density reconstruction offers a significantly detailed depiction of the cosmic density field, allowing for the detection of less prominent filaments that the DTFE method misses. This scenario resembles our approach, where a reduction in $R_{\rm s}$ improves the cosmological density resolution, allowing the identification of subtler filaments and producing a flatter trend for smaller $R_{\rm s}$ values.

This research sets itself apart with distinctive methodological techniques and constrained simulations that enhance our understanding of the influence of cosmic filaments on galaxy evolution. Unlike many studies that use algorithms like DisPerSE or NEXUS (which often focus on density ridges or topological persistence), this work employs the COWS method to define filaments as medial axes (skeletons) of the cosmic web. The study uniquely pairs SDSS observations with the ELUCID simulation, a constrained dark-matter-only simulation reconstructed to match the observed local Universe (for example, galaxy groups and filaments). Unlike random cosmological simulations, the alignment of ELUCID with the real universe minimizes sampling bias, enabling direct statistically robust comparisons between simulations and observations. The summary of our findings is presented below.

(i) As galaxies or central subhaloes approach closer to the filaments, their masses tend to increase, especially when higher values for the parameters $R_{\rm s}$ or $\lambda_{\rm th}$ are used in the filament classification technique.

(ii) Galaxies that are situated close to the filament axes generally display a redder colour and usually present lower sSFRs. Subhaloes within a certain mass range are typically older when located near the core areas of filaments, particularly for $R_{\rm s} = 4.0\,h^{-1}$Mpc or $\lambda_{\rm th} = 0.8$.

(iii) The study uses the GZ2 catalogue to classify galaxies as elliptical or spiral. The findings indicate a higher proportion of elliptical galaxies compared to spirals closer to the filament axes, particularly evident for $R_{\rm s} = 4.0\,h^{-1}$Mpc or $\lambda_{\rm th} = 0.8$.

(iv) Galaxies with lower mass are typically smaller in size when located near the filament spines. In contrast, galaxies of higher mass, specifically those with $\log(M_*/(\,h^{-2}{\rm M}_{\odot})) \geq 10.5$, tend to become larger as they approach the filament axes. The pattern found in the half-mass radii $R_{1/2}$ of haloes positioned close to filaments is similar to the trend observed in the half-light radii R_{50} of galaxies.

(v) In general, as haloes approach filaments, their concentration or spin tends to increase. This suggests that the cosmic web exerts a notable influence on the dynamics of haloes.

In conclusion, this research uses the COWS method to detect cosmic web structures, revealing that the properties of galaxies or haloes are significantly affected by their distance to cosmic filaments. The results support the notion that the large-scale structure of Universe, characterized by cosmic filaments, plays a vital role in shaping galaxy and halo properties, which are consistent with patterns noted in previous research. Motivated by this, upcoming studies will investigate the ways in which galaxy or halo characteristics are affected and evolved along the evolution of the cosmic web, from cosmic void, sheet, to filament, and then clusters.

It is important to note that different filament detection algorithms may produce a variety of distinct results. For example, the COWS method evaluates the properties of galaxies beginning at a distance of $0.5\,h^{-1}$Mpc from the filament's axis. This approach uses a grid structure to establish the axis of the filament, with the finest resolution being equivalent to the grid's size. However, using the axis determined by DisPerSE, calculations can be performed efficiently within $0.5\,h^{-1}$Mpc. In particular, the DisPerSE method indicates that the boundary of the filament, as described in Wang et al. (2024b), is roughly 1Mpc. Besides the difficulty of defining the filament axis, there are other factors that could be significant. In the COWS approach, altering the parameters $R_{\rm s}$ and $\lambda_{\rm th}$ in the filament catalogue

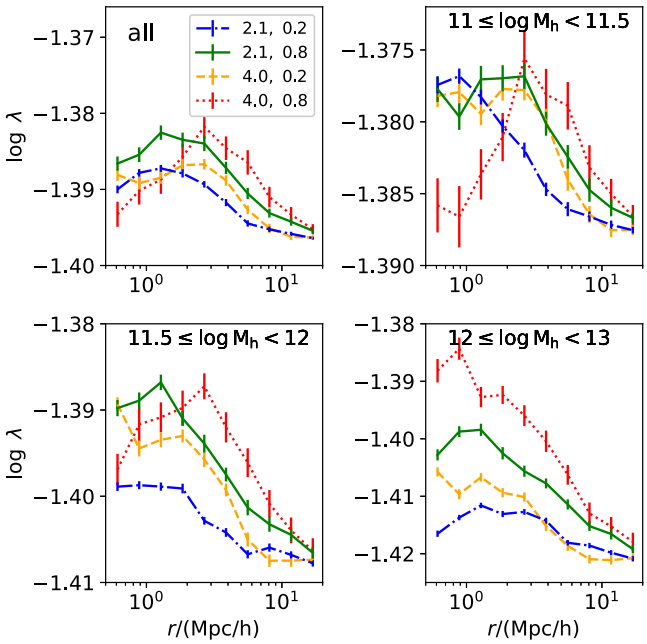

Figure 13. Similar to Fig. 12, but for the halo spin parameter λ.

results in variations in the distribution of characteristics among the galaxies surrounding the filaments. Alternative methods employed to detect filaments are also likely to affect how galaxy features are distributed around these filaments. In forthcoming studies, we plan to explore how various filament detection techniques influence galaxy properties.

ACKNOWLEDGEMENTS

This research is funded by various grants, including the National SKA Program of China (grant no. 2020SKA0110100), the National Natural Science Foundation of China (no. 12273088), and the National Key R&D Programme of China (2023YFA1607800, 2023YFA1607804). Additional support comes from the CSST project (no. CMS-CSST-2021-A02), the CAS Project for Young Scientists in Basic Research (no. YSBR-092), Fundamental Research Funds for Central Universities, the 111 project (no. B20019), and the Shanghai Natural Science Foundation (grant nos. 19ZR1466800, 23JC1410200, ZJ20223-ZD-003). PW acknowledge financial support by the NSFC (no. 12473009), and also sponsored by Shanghai Rising-Star Program (no. 24QA2711100).

This work is also supported by the High-Performance Computing Resource in the Core Facility for Advanced Research Computing at Shanghai Astronomical Observatory.

This work used ASTROPY: a community-developed core Python package and an ecosystem of tools and resources for astronomy (Astropy Collaboration 2013, 2018, 2022).

Funding for the SDSS IV has been provided by the Alfred P. Sloan Foundation, the U.S. Department of Energy Office of Science, and the Participating Institutions. SDSS acknowledges support and resources from the Centre for High-Performance Computing at the University of Utah. The SDSS website is www.sdss.org.

SDSS is managed by the Astrophysical Research Consortium for the Participating Institutions of the SDSS Collaboration including the Brazilian Participation Group, the Carnegie Institution for Science, Carnegie Mellon University, the Chilean Participation Group, the French Participation Group, Harvard-Smithsonian Center for Astrophysics, Instituto de Astrofísica de Canarias, The Johns Hopkins University, Kavli Institute for the Physics and Mathematics of the Universe (IPMU)/University of Tokyo, Lawrence Berkeley National Laboratory, Leibniz Institut für Astrophysik Potsdam (AIP), Max-Planck-Institut für Astronomie (MPIA Heidelberg), Max-Planck-Institut für Astrophysik (MPA Garching), Max-Planck-Institut für Extraterrestrische Physik (MPE), National Astronomical Observatories of China, New Mexico State University, New York University, University of Notre Dame, Observatório Nacional/ MCTI, The Ohio State University, Pennsylvania State University, Shanghai Astronomical Observatory, United Kingdom Participation Group, Universidad Nacional Autónoma de México, University of Arizona, University of Colorado Boulder, University of Oxford, University of Portsmouth, University of Utah, University of Virginia, University of Washington, University of Wisconsin, Vanderbilt University, and Yale University.

DATA AVAILABILITY

The data underlying this article will be shared on reasonable request with the corresponding author.

REFERENCES

Abazajian K. N. et al., 2009, ApJS, 182, 543
Alpaslan M. et al., 2014, MNRAS, 438, 177
Alpaslan M. et al., 2015, MNRAS, 451, 3249
Astropy Collaboration, 2013, A&A, 558, A33
Astropy Collaboration, 2018, AJ, 156, 123
Astropy Collaboration, 2022, ApJ, 935, 167
Bell E. F., McIntosh D. H., Katz N., Weinberg M. D., 2003, ApJS, 149, 289
Blanton M. R. et al., 2001, AJ, 121, 2358
Blanton M. R. et al., 2005, AJ, 129, 2562
Bond J. R., Kofman L., Pogosyan D., 1996, Nature, 380, 603

Bonjean V., Aghanim N., Douspis M., Malavasi N., Tanimura H., 2020, A&A, 638, A75
Bryan G. L., Norman M. L., 1998, ApJ, 495, 80
Bulichi T.-E., Davé R., Kraljic K., 2024, MNRAS, 529, 2595
Carrón Duque J., Migliaccio M., Marinucci D., Vittorio N., 2022, A&A, 659, A166
Cautun M., van de Weygaert R., Jones B. J. T., 2013, MNRAS, 429, 1286
Cautun M., van de Weygaert R., Jones B. J. T., Frenk C. S., 2014, MNRAS, 441, 2923
Chang Y.-Y., van der Wel A., da Cunha E., Rix H.-W., 2015, ApJS, 219, 8
Chen Y.-C. et al., 2017, MNRAS, 466, 1880
Chen Y., Mo H. J., Li C., Wang H., Yang X., Zhou S., Zhang Y., 2019, ApJ, 872, 180
Cochrane R. K. et al., 2023, MNRAS, 523, 2409
Conrado A. M. et al., 2024, A&A, 687, A98
Cooper M. C. et al., 2012, MNRAS, 419, 3018
Curtis O., McDonough B., Brainerd T. G., 2024, ApJ, 962, 58
da Cunha E., Charlot S., Elbaz D., 2008, MNRAS, 388, 1595
Darvish B., Sobral D., Mobasher B., Scoville N. Z., Best P., Sales L. V., Smail I., 2014, ApJ, 796, 51
Davis M., Efstathiou G., Frenk C. S., White S. D. M., 1985, ApJ, 292, 371
DESI Collaboration, 2024, AJ, 168, 58
Domínguez-Gómez J. et al., 2023, A&A, 680, A111
Donnan C. T., Tojeiro R., Kraljic K., 2022, Nat. Astron., 6, 599
Figueira M., Siudek M., Pollo A., Krywult J., Vergani D., Bolzonella M., Cucciati O., Iovino A., 2024, A&A, 687, A117
Hahn O., Porciani C., Carollo C. M., Dekel A., 2007, MNRAS, 375, 489
Hasan F. et al., 2023, ApJ, 950, 114
Hasan F. et al., 2024, ApJ, 970, 177
Hoosain M. et al., 2024, MNRAS, 528, 4139
Hoyle F., Rojas R. R., Vogeley M. S., Brinkmann J., 2005, ApJ, 620, 618
Hoyle F., Vogeley M. S., Pan D., 2012, MNRAS, 426, 3041
Jiang F. et al., 2019, MNRAS, 488, 4801
Khochfar S., Silk J., 2006, ApJ, 648, L21
Kleiner D., Pimbblet K. A., Jones D. H., Koribalski B. S., Serra P., 2017, MNRAS, 466, 4692
Kraljic K. et al., 2018, MNRAS, 474, 547
Kreckel K., Croxall K., Groves B., van de Weygaert R., Pogge R. W., 2015, ApJ, 798, L15
Kroupa P., 2001, MNRAS, 322, 231
Kuutma T., Tamm A., Tempel E., 2017, A&A, 600, L6
Laigle C. et al., 2018, MNRAS, 474, 5437
Lee T., Kashyap R., Chu C., 1994, CVGIP: Graphical Models and Image Processing, 56, 462
Lu Y. S., Mandelker N., Oh S. P., Dekel A., van den Bosch F. C., Springel V., Nagai D., van de Voort F., 2024, MNRAS, 527, 11256
Luber N., van Gorkom J. H., Hess K. M., Pisano D. J., Fernández X., Momjian E., 2019, AJ, 157, 254
Luo X. et al., 2024, ApJ, 966, 236
Malavasi N. et al., 2017, MNRAS, 465, 3817
Malavasi N., Aghanim N., Douspis M., Tanimura H., Bonjean V., 2020, A&A, 642, A19
Meert A., Vikram V., Bernardi M., 2015, MNRAS, 446, 3943
Montero-Dorta A. D., Rodriguez F., 2024, MNRAS, 531, 290
Naab T., Johansson P. H., Ostriker J. P., 2009, ApJ, 699, L178
Navarro J. F., Frenk C. S., White S. D. M., 1997, ApJ, 490, 493
O'Kane C. J., Kuchner U., Gray M. E., Aragón-Salamanca A., 2024, MNRAS, 534, 1682
Old L. J. et al., 2020, MNRAS, 493, 5987
Pakmor R. et al., 2023, MNRAS, 524, 2539
Parente M. et al., 2024, ApJ, 966, 154
Pasha I., Mandelker N., van den Bosch F. C., Springel V., van de Voort F., 2023, MNRAS, 520, 2692
Peebles P. J. E., 1967, ApJ, 147, 859
Peebles P. J. E., 1969, ApJ, 155, 393
Pfeifer S., Libeskind N. I., Hoffman Y., Hellwing W. A., Bilicki M., Naidoo K., 2022, MNRAS, 514, 470
Romeo A. B., Agertz O., Renaud F., 2023, MNRAS, 518, 1002
Rosas-Guevara Y., Tissera P., Lagos C. d. P., Paillas E., Padilla N., 2022, MNRAS, 517, 712
Rost A., Stasyszyn F., Pereyra L., Martínez H. J., 2020, MNRAS, 493, 1936
Rowntree A. R. et al., 2024, MNRAS, 531, 3858
Salerno J. M. et al., 2020, MNRAS, 493, 4950
Sarron F., Adami C., Durret F., Laigle C., 2019, A&A, 632, A49
Simard L., Mendel J. T., Patton D. R., Ellison S. L., McConnachie A. W., 2011, ApJS, 196, 11
Sousbie T., 2011, MNRAS, 414, 350
Sousbie T., Pichon C., Kawahara H., 2011, MNRAS, 414, 384
Springel V., 2005, MNRAS, 364, 1105
Springel V., White S. D. M., Tormen G., Kauffmann G., 2001, MNRAS, 328, 726
Taamoli S. et al., 2024, ApJ, 966, 18
Tugay A., Tarnopolski M., 2023, ApJ, 952, 3
Tweed D., Yang X., Wang H., Cui W., Zhang Y., Li S., Jing Y. P., Mo H. J., 2017, ApJ, 841, 55
Vulcani B. et al., 2019, MNRAS, 487, 2278
Wang H. et al., 2016, ApJ, 831, 164
Wang H. et al., 2018, ApJ, 852, 31
Wang H., Mo H. J., Yang X., Jing Y. P., Lin W. P., 2014, ApJ, 794, 94
Wang H., Mo H. J., Yang X., van den Bosch F. C., 2012, MNRAS, 420, 1809
Wang W. et al., 2024b, MNRAS, 532, 4604
Wang Z., Shi F., Yang X., Li Q., Liu Y., Li X., 2024a, Sci. China Phys. Mech. Astron., 67, 219513
Wechsler R. H., Tinker J. L., 2018, ARA&A, 56, 435
Wegner G. A., Salzer J. J., Taylor J. M., Hirschauer A. S., 2019, ApJ, 883, 29
Willett K. W. et al., 2013, MNRAS, 435, 2835
Winkel N., Pasquali A., Kraljic K., Smith R., Gallazzi A., Jackson T. M., 2021, MNRAS, 505, 4920
Woo J. et al., 2013, MNRAS, 428, 3306
Wright E. L. et al., 2010, AJ, 140, 1868
Xue W., Rong Y., Hua Z., 2024, preprint (arXiv:2411.11443)
Yang T., Hudson M. J., Afshordi N., 2022, MNRAS, 516, 6041
Yang X. et al., 2018, ApJ, 860, 30
Yang X., Mo H. J., van den Bosch F. C., Pasquali A., Li C., Barden M., 2007, ApJ, 671, 153
Yang X., Mo H. J., van den Bosch F. C., Zhang Y., Han J., 2012, ApJ, 752, 41
York D. G. et al., 2000, AJ, 120, 1579
Zakharova D., Vulcani B., De Lucia G., Xie L., Hirschmann M., Fontanot F., 2023, MNRAS, 525, 4079
Zhang T. Y., Suen C. Y., 1984, Commun. ACM, 27, 236–239
Zhang Y.-C., Yang X.-H., 2019, Res. Astron. Astrophys., 19, 006
Zhang Y., Guo H., Yang X., Wang P., 2024, MNRAS, 533, 1048
Zhang Y., Yang X., Faltenbacher A., Springel V., Lin W., Wang H., 2009, ApJ, 706, 747
Zhang Y., Yang X., Guo H., 2021a, MNRAS, 500, 1895
Zhang Y., Yang X., Guo H., 2021b, MNRAS, 507, 5320
Zhang Y., Yang X., Guo H., 2022, MNRAS, 517, 3579
Zhang Y., Yang X., Wang H., Wang L., Luo W., Mo H. J., van den Bosch F. C., 2015, ApJ, 798, 17
Zhang Y., Yang X., Wang H., Wang L., Mo H. J., van den Bosch F. C., 2013, ApJ, 779, 160
Zhao D. H., Jing Y. P., Mo H. J., Börner G., 2009, ApJ, 707, 354

This paper has been typeset from a TEX/LATEX file prepared by the author.